Article:

Dorrell, RM, Peakall, J, Burns, C et al. (1 more author) (2018) A novel mixing mechanism in sinuous seafloor channels: Implications for submarine channel evolution. Geomorphology, 303. pp. 1-12. ISSN 0169-555X

https://doi.org/10.1016/j.geomorph.2017.11.008

A novel mixing mechanism in sinuous seafloor channels: implications for submarine channel evolution

R.M. Dorrell[1*], J. Peakall[2], C. Burns[2], G.M. Keevil[2]

[1] Energy and Environment Institute, University of Hull, Hull, HU6 7RX.

[2] School Earth and Environment, University of Leeds, Leeds, LS2 9JT.

[*] r.dorrell@hull.ac.uk

Abstract

Previous experimental studies of density currents in sinuous seafloor channels have almost exclusively studied hydrodynamics either by considering time independent, instantaneous, flow measurements or by compiling time-averaged flow measurements. Here we present a novel study of the time dependent dynamics of a density driven flow in a sinuous channel fed by a source of constant discharge. The experiments show that whilst source conditions may be temporally steady, flow conditions are temporally unsteady with timescales of flow variation driven by flow interaction with channel topography. Temporal variations reveal that both downstream and cross-stream flows vary significantly from time average observations and predictions, across scales larger than those predicted for turbulence in equivalent straight channels. Large-scale variations are shown to increase the average production of turbulence across the height of the flow, providing a new mechanism for enhanced mixing of sediment within gravity currents. Further such large scale variations in flow conditions are recorded in the change in orientation of near-bed secondary flow, providing a plausible mechanism to reduce the cross-stream transport of bedload material and explain the ultimate stabilisation of sinuous seafloor channel systems.

1 Introduction

Density driven flows, such as turbidity currents, build and maintain sinuous channels on the seafloor that can extend for hundreds or thousands of kilometres (Wynn et al., 2007; Straub et al., 2008; Dorrell et al., 2015). Networks of these channels form the largest sedimentary landforms on the planet: submarine fans (Covault, 2011). The extent of mixing of suspended particulate material by turbulent flow is known to provide a key control on the degree to which the sediment suspension is stratified in these density-driven flows, yet stratification is also known to be a key control influencing the extent to which these flows may propagate over such large distances (Dorrell et al., 2014). As in rivers, the mechanisms of mixing include: shear generated turbulence; unstable buoyancy gradient generated turbulence; secondary (i.e., rotational) flow; particle-particle interaction; and, Brownian motion. However, in contrast to rivers (where the velocity tends to increase monotonically with distance from the bed), turbulence in straight-channel, steady-state density driven flows is observably reduced at the height of the downstream velocity maximum; because at this point shear generated turbulence production reduces to zero (Garcia and Parker, 1993; Kneller et al., 1999; Best et al., 2001; Buckee et al., 2001). This zone of reduced shear has been termed the slow diffusion zone and is postulated as being an internal barrier to sediment transport (Garcia and Parker, 1993; Kneller et al., 1999; Best et al., 2001; Buckee et al., 2001). Previous work has suggested that there are a number of mechanisms that operate in sinuous submarine channels that act to reduce the influence of this slow diffusion zone: i) induced secondary flow that mixes fluid vertically (Keevil et al., 2006); ii) flow run-up and superelevation that again act to move fluid vertically within the flow (Straub et al., 2011); and iii) internal hydraulic jumps within channels that generate large upward vertical velocities, redistributing mass and momentum (Dorrell et al., 2016). Here we demonstrate a new mechanism for mixing across the slow diffusion zone in density currents in sinuous submarine channels, linked to temporal changes in the structure of secondary flow fields. This novel mixing mechanism is believed to be unique to sinuous submarine channels, with no equivalent in river systems. Furthermore, these temporal changes in secondary flow have significant implications for bedload transport and channel evolution.

Secondary flow, which rotates normal to the primary flow downstream, is ubiquitous in straight and sinuous channels (Nezu and Nakagawa, 1993; Peakall and Sumner, 2015). However, in sinuous channels the magnitude of secondary flow, and thus its affect on flow dynamics is enhanced, by centrifugal and pressure gradient forces driving recirculating flow. In sinuous open channels the near-bed component of secondary flow is typically orientated towards the inner-bank of the channel bend at bend apices (Rozovskii, 1957; Thorne et al., 1985). However, in density driven flows near-bed secondary flow is more complex; here secondary flow at bend apices may be orientated towards the inner- or outer-bank and may be composed of either single flow cells, or multiple, vertically stacked, cells (Kassem and Imran, 2004; Corney et al., 2006, 2008; Keevil et al., 2006; Abad et al., 2011; Dorrell et al., 2013). By redistributing suspended and bedload sediment, secondary flow plays a key role in the morphodynamic evolution of sinuous channel systems (Peakall et al., 2007; Darby and Peakall, 2012; Cossu and Wells, 2013; Peakall and Sumner, 2015).

In unstratified open-channel flow inner bank orientated secondary flow is driven by a balance of outer-bank orientated centrifugal forces, reduced near the bed by friction, and an inner-bank orientated pressure gradient, resulting from flow superelevation (Rosovskii, 1957). However, in density driven flows this force balance is modified by density and velocity stratification (Corney et al., 2006, 2008; Abad et al., 2011), enhanced superelevation, and associated flow overspill from the channel (Dorrell et al., 2013; Ezz and Imran, 2014). Moreover, in large channels at high latitudes the secondary flow is also significantly affected, and may be reversed, by Coriolis forcing (Cossu and Wells, 2010; Cossu et al., 2015).

Dorrell et al. (2013) demonstrated that secondary flow in temporally steady density currents is dominated by flow superelevation, and overspill (if present), reflected in the magnitudes of the dimensionless radial fluid, Q_f and radial material, Q_s, fluxes (Figure 1), defined by

(1a) $Q_f = \frac{\int_0^h V \mathrm{dz}}{h}$,

(1b) $Q_s = \frac{\int_0^h V(\rho_f - \rho_a)\mathrm{dz}}{\int_0^h (\rho_f - \rho_a)\mathrm{dz}}$,

(1c) $V = \frac{L\mu v}{\rho_a \left(\int_0^h \mathrm{udz}\right)^2}$.

In Equation (1) the variables are defined as follows: L, the horizontal length scale of the flow (i.e. radius of curvature); h, the vertical length scale of the flow (i.e. the flow depth); u and v, the down- and cross-stream components of flow velocity, where V denotes the dimensionless secondary flow velocity; μ, dynamic fluid viscosity; and ρ_f and ρ_a, the density of the flow, and ambient fluid, respectively. Due to differences in the mechanisms driving vertical density and velocity stratification these fluxes may have significantly different magnitudes. As the concentration of suspended material is known to increase towards the bed (Menard and Ludwick, 1951; Peakall et al., 2000a), and the secondary flow peaks near the height of the downstream velocity maximum (Abad et al., 2011) the depth-averaged radial material flux is likely to be greater than the radial fluid flux (Dorrell et al., 2013). Consequently it has been speculated that basal drag, affecting elevation of the velocity maximum, has a significant effect on secondary flow (Abad et al., 2011). Furthermore, as the density difference between the flow and the ambient fluid is small in density currents, flow superelevation in submarine channels is an order of magnitude, or more, larger than in open-channel flows (Imran et al., 1997). This superelevation, in combination with flow overspill means that the relative magnitude of both the radial fluid and material fluxes is significantly enhanced, preferentially towards the outer-bank.

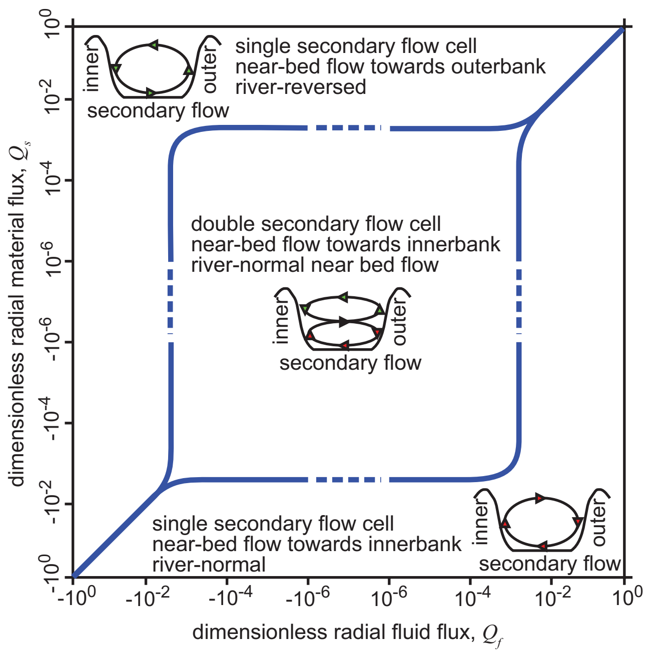

Figure 1. The phase space solution for the dynamics of secondary flow, as a function of cross-channel (radial) fluid and material fluxes (see Equation 1), modified after Dorrell et al. (2013).

Stratified buoyancy driven gravity currents are known to be inherently unstable to topographic perturbations (Baines, 1998; Sakar and Scotti, 2017), in contrast to open-channel flows. Consequently, it is anticipated that the resulting large-scale temporal variations in gravity currents would lead to significant changes between instantaneous and time-averaged flow fields, for both primary and secondary flows. In turn, these fluctuations and in particular any divergences in flow direction between instantaneous and time-averaged flows would be expected to have important implications for flow, mixing, and sediment transport. Despite this, previous modelling of secondary flow within sinuous seafloor channels has exclusively focused on the mean flow dynamics of nominally steady state flows, and has consequently considered mixing processes solely in terms of these time-averaged flow dynamics. This paper seeks to use experimental observations to: i) examine the nature of temporal changes in secondary flow dynamics, and their role in mixing, ii) assess secondary flow dynamics as a function of net radial fluid-fluxes and basal drag, as parameterised by bed surface roughness, iii) provide a process-based model for temporal variations in secondary flow, and, iv) explore the implications of temporal variations in secondary flow and associated mixing, in terms of intra-channel sedimentation, submarine channel evolution, and flow runout.

2 Methodology

2.1 Experimental Methodology

A series of experiments were undertaken in a flume tank that is 1.8 m square, and 1.7 m deep, with a 2 m straight inflow channel on the upstream face (see Figure 2). The tank has a false floor placed 0.4 m above the tank bottom to create a sump; consequently gravity currents reaching the end of the floor drop into the sump and do not undergo reflection from the sidewalls. A preformed channel model with a sinuosity of 1.36 was placed in the tank and connected to the inflow channel. The channel model consisted of bends of constant radius, over an arc of 120°, connected by straight sections (see Figure 2), identical to the planform used in the gravity current experiments of Keevil et al. (2006, 2007). The planform setup of the channel was based on the UK Flood Channel Facility meanders (Greenhill and Sellin, 1993; Sellin et al., 1993). The channel model had a rectangular cross-section, with a width of

0.12 m, and sides that were 0.40 m high so that the flow was fully confined with an absence of overspill.

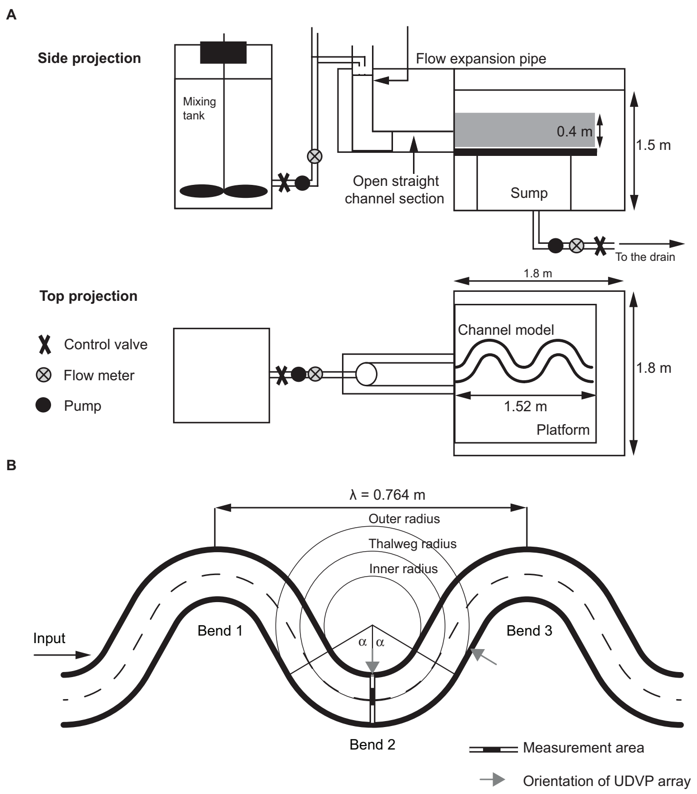

Figure 2. (a) Schematic sketch of the experimental setup, illustrating the mixing tank and the position of the channel model within the main flume tank. (b) Planform geometry of the channel model illustrating all the elements in a single wavelength. The actual channel model consists of two complete wavelengths, covering three bends; each bend has an angle of curvature (α) of 60°. The channel has a sinuosity of 1.36 and a constant cross-sectional width; with an inner radius of 0.1 m, thalweg radius of 0.16 m and outer radius of 0.22 m.

A saline solution with a 2.5% density excess (1025 kg m^{-3}) was prepared in a 1.8 m^3 mixing tank and pumped into the model via the straight inlet channel at a flow rate of 1.13 l s^{-1}. As the dense fluid entered the tank it passed through an expansion pipe to reduce the turbulence on the inlet, and then through a straight channel, 0.12 m wide and with a development length of 1.3 m long, connected to the main sinuous channel.

Velocity measurements were taken at the second bend apex, using an array of ten 4 MHz ultrasonic Doppler velocity profiling (UDVP) probes, positioned at heights of: 6 (0.05h), 16 (0.09h), 26 (0.21h), 36 (0.28h), 46 (0.36h), 56 (0.44h), 76 (0.60h), 96 (0.76h), 116 (0.92h) and 136 (1.08h) mm above the channel floor (parentheses denote the dimensionless depth of the UDVP probe in terms of the mean flow height, of h=126 mm, see Table 1). Cross-stream flow was measured with the array positioned into and flush with the sidewall, with the probes positioned on the inner bank of the bend. Similarly downstream flow was measured by an upstream-facing array mounted in a bespoke PVC probe holder, and positioned 4 cm downstream of the bend apex, so that the UDVP profiles intersected the centreline of the channel at the bend apex.

UDVP measures single component velocity in the direction in which the probes are orientated and works by emitting ultrasonic pulses and then gating the return signal into a series of spatial bins (here 128 bins), as the ultrasound backscatters off of small particles within the flow (Best et al., 2001). The probes operate individually, and are multiplexed enabling pseudo-instantaneous velocity fields to be constructed, in this case at a frequency of 3.33 Hz. Cross-stream and downstream velocities were measured in separate nominally identical runs, to avoid cross-talk between instruments. Cross-steam and downstream spatial return bin sizes were set at 1.48 mm, with downstream velocity averaged from the 5 bins central to the bend apex. To remove any velocity spikes, all the instantaneous velocity data were filtered by two standard deviations from a 11-point moving mean and the points were replaced with a 3-point moving mean (Buckee et al., 2001). As compiled datasets from the arrayed UDVP probes varied both spatially and temporally. Matlab's™ griddata function was used to interpolate spatial variation of the flow at fixed time, assuming a zero-slip velocity boundary condition on the height of the various bed roughnesses used in the experiments.

Eighteen experimental runs were undertaken in the flume with either the cross-stream or downstream UDVP probes active. In the subsequent analysis, each pair of repeat runs (downstream and cross-stream) is referred to as a single experiment, giving experiments I to IX. Three variations in bed roughness were chosen by building a fixed bed composed of: fine sand d_{50} =186 μm, coarse sand

d_{50} = 370 μm and very coarse glass spheres of 6 mm diameter. For each variation in bed roughness the entire tank was set at either 1°, 2°or 3° and the water level in the tank filled to 1.4 m. Velocity measurements were started 30 s after the flow had traversed the length of the sinuous channel; 500 cycles were recorded, resulting in a relative sample time t = 0 to 150 s, at which point the experiment was stopped.

The planform channel setup and experimental slopes considered are not designed to mimic any specific environmental setup. However, the deep channel sidewalls used mean the experiments are most characteristic of sinuous incised channels (confined flows) found on continental slopes and in some isolated deep-ocean channels on basin floors, or non-overspilling flows in aggradational submarine fan channels (Peakall and Sumner, 2015).

Table 1. Flow parameters, time averaged for t=0 to 150 s, for experimental runs I-IX.

Run	I	II	III	IV	V	VI	VII	VIII	IX
d_{50}, *mm*	0.19	0.19	0.19	0.37	0.37	0.37	6.00	6.00	6.00
s	1°	2°	3°	1°	2°	3°	1°	2°	3°
$\tilde{u}$, mm/s	67.5	71.6	75.9	65.8	70.1	73.0	66.9	70.2	74.5
$\tilde{v}$, mm/s	8.28	12.9	14.4 s	7.39	10.4	14.2	11.6	12.6	15.4
h, mm	128	126	128	123	131	124	126	126	126
C_d	0.119	0.209	0.284	0.121	0.227	0.297	0.120	0.218	0.291
Fr_d	0.381	0.408	0.429	0.378	0.391	0.419	0.380	0.400	0.423
Re	8620	9000	9690	8130	9150	9050	8450	8830	9420

2.2 Flow Analysis and Characterisation

Recorded downstream (primary), u, inner- to outer-bank cross-stream (secondary), v, and derived vertical, w, flow velocities are separated into long-term average, denoted by overbar notation, and fluctuating components, denoted by prime notation,

(2) $u = \bar{u} + u'$, $v = \bar{v} + v'$ and $w = \bar{w} + w'$.

Observed velocities of each experimental run characterise individual experimental configurations, as summarised in Table 1. To calculate the flow height from the separate one-component down- and cross-stream velocity datasets two different methodologies are necessarily employed. When using the downstream flow data, the flow height is defined by the height at which the downstream flow velocity is zero (see Figure 3 and Dorrell et al., 2014); conversely when using the cross-stream velocity data the flow height is defined by the position where the vertical gradient of the secondary flow velocity profile is zero, i.e. the zero shear condition (see Figure 3 and Abad et al., 2011). The excess buoyancy of the flow is defined as $g' = g(\rho_f/\rho_a - 1)$; where the flow density $\rho_f = 1025$ kg m^{-3} and the ambient fluid density $\rho_a = 1000$ kg m^{-3}. The densimetric Froude number of the flow (Baines, 1998; Kneller and Buckee, 2000) is given by the dimensionless ratio of depth-averaged inertial to gravitational forces

(3) $$Fr_d = \frac{\tilde{u}}{\sqrt{g'h}},$$

where tilde notation denotes depth and time average velocity, $\tilde{u} = \int_0^h \bar{u}dz/h$, see Table 1. Given the fluid viscosity, μ, the Reynolds number defines the ratio of momentum to viscous forces,

(4) $$Re = \frac{\rho_a \tilde{u} h}{\mu},$$

As Re>8000 in the experiments conducted here, see Table 1, all flows are considered fully turbulent. Further, the frictional drag, C_d, suffered by a flow with basal slope, s, is estimated by the Parker et al., (1987) frictional-entrainment-gravitational force balance

(5) $$s = \frac{C_d + E\left(1 + \frac{1}{2}Fr_d^{-2}\right)}{Fr_d^{-2}},$$

where ambient fluid-entrainment, E, is calculated by the empirical formula of Fukushima et al., (1985)

(6) $$E = \frac{0.00153}{0.0204 + Fr_d^{-2}}.$$

Finally, cross-channel vertical flow velocities are derived under the simplifying assumption that, at the bend apex, downstream variations in the flow are negligible. Given the observed secondary flow field at the bend apex, mass conservation implicitly defines vertical flow velocity by the leading order differential equation,

(7) $$\frac{\partial v}{\partial y} + \frac{\partial w}{\partial z} = 0,$$

which is solved subject to a no-slip boundary condition, w=0, at the bed roughness height z=z_0 taken as the diameter, d, of particles attached to the solid bed.

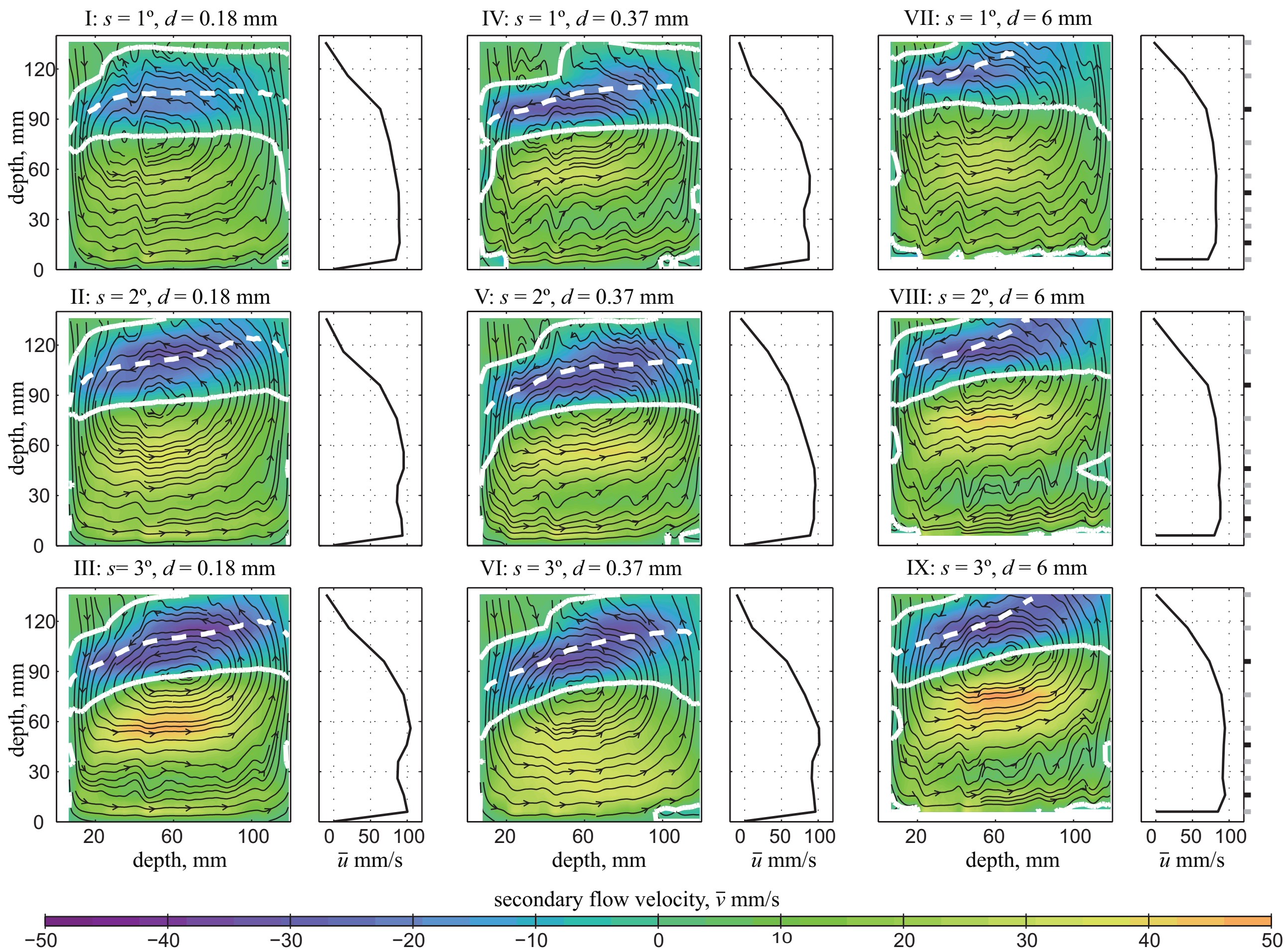

Figure 3. The primary (downstream), $\bar{u}$, and secondary (cross-stream), $\bar{v}$, velocity flow fields in experiments I-IX, time averaged over t=0 to 150 s (Table 1). Contour maps of secondary velocity are orientated from inner (left) to outer (right) bank. Outerbank flow is described as positive. Downstream flow is derived from an average taken across the radial centreline of the apex. Black lines denote flow streamlines; solid white lines denote contours of zero velocity; dashed white lines denote contours of zero shear, used to define flow depth. Note the blanking distance at the base of experiments VII-IX caused by the 6 mm glass sphere bed-roughness elements. Grey and black tick marks on VII, VIII and IX denote UDVP location.

3 Results

3.1 Temporally averaged secondary flow dynamics.

The long-term time average flow velocities, taken over 150 s, of experiments I-IX are shown in Figure 3 and Table 1. The nine experiments show the effect of varying background slope and bed roughness on average flow structure. Contour plots are used to show the structure of the secondary (cross-channel) flow velocity; whilst primary (downstream) flow velocity profiles are derived at the centre point of the bend apex. As noted above, primary and secondary flow velocities were recorded in separate experimental runs so are not quantitatively comparable.

From Figure 3 it is observed that around the midpoint of the flow depth, down towards the base of the flow, the average primary flow velocity is plug-like; with the velocity decreasing due to frictional shear close to the bed, and towards the flow-ambient fluid interface. The size of the plug-like region increases with decreasing bed roughness, (therefore with decreasing basal shear), and decreasing slope leading to reduced gravitational acceleration and associated turbulent mixing and frictional shear at the flow-ambient fluid boundary. The secondary flow velocity maps, Figure 3, also show that the maximum outer-bank orientated flow is located near the mid-point of the flow. Below this maximum there is a local minimum, where flow is still orientated towards the outer-bank, with the magnitude of flow towards the outer-bank then increasing again closer to the bed. Above the outer-bank orientated velocity maximum the secondary flow decreases, becoming negative and orientated towards the inner-bank. The lower, outer-bank orientated, and upper, inner-bank orientated, flow show that averaging leaves a single secondary flow cell rotating in the reverse direction to those of fluvial systems (Rosovskii, 1957). The long-term average rotation pattern of the secondary flow at the bend apex is emphasised by the estimation of vertical flow velocities (Equation 7), enabling flow streamlines to be determined.

Figure 3 shows that with increased bed-roughness, average near-bed flow may decrease and become inner bank orientated, i.e. river-normal (Abad et al., 2011; Dorrell et al., 2013). However, such river-normal near-bed flow was predominately observed to be located near the sidewalls, see, e.g., Figure 3 I-VI. Although bed roughness was doubled between experiments I-III and IV-VI (the size of particles comprising the immobile bed increased from ~0.15% to ~0.30% of mean flow depth) cross-stream flow remained similar. However, near bed flow orientated towards the inner bank (located away from the sidewalls) was observed in the very coarse bed experiments, Figure 3 VII-IX, where the size of particles comprising the immobile bed was ~5% of the mean flow depth. Bed roughness has been suggested as a key parameter determining the orientation of secondary flow, as lower roughness is linked to a reduction in the height of the velocity maximum, therefore encouraging river-reversed circulation (Abad et al., 2011). Smooth beds as used in some experiments (e.g., Corney et al., 2006; Keevil et al., 2006, 2007) were therefore argued to exhibit 'anomalous' river-normal secondary flows (Abad et al., 2011). However, here the results show that beds with grain-roughnesses (0.15-0.30%) far in excess of those expected for sand-bed channelized flows in natural systems, still exhibit river-reversed patterns, and that extreme roughness is required (~5% of flow depth) in the present experiments before roughness begins to alter the orientation of the basal flow velocities. This is in agreement with previous experiments which did not recognise bed roughness as an important parameter controlling secondary flow orientation (Ezz and Imran, 2014). Figure 3 also shows that with increased bed-roughness, and basal slope, the slope of the flow-ambient fluid interface increased. Moreover, with increased basal slope the centre of secondary flow circulation is observed to move towards the outer-bank (Keevil et al., 2007).

3.2 Temporally varying secondary flow dynamics.

The difference between the flow velocity at a given point in time and its long-term average is the flow velocity fluctuation, Equation (2). In Figure 4 the velocity fluctuations of the downstream and cross-stream flow, recorded in run V, are presented for the UDVP located above the velocity maximum (z = 96 mm), near the velocity maximum (z = 46 mm) and below the velocity maximum (z = 16 mm) (locations UDVPs used in Figure 4 are highlighted in Figure 3). Velocity fluctuations for all 10 UDVP probes are presented in the supplementary material. The velocity fluctuations are chaotic, as expected due to turbulent fluid motion, but also show long-term periodic variations. Due to the low frequency of the UDVP array (~3 Hz) high frequency small-scale turbulent structures are not resolved. However, by taking a Fast Fourier Transform (FFT) of the velocity fluctuations low frequency forcing on both the primary and secondary flow fields are observed between 0.05-0.2 Hz.

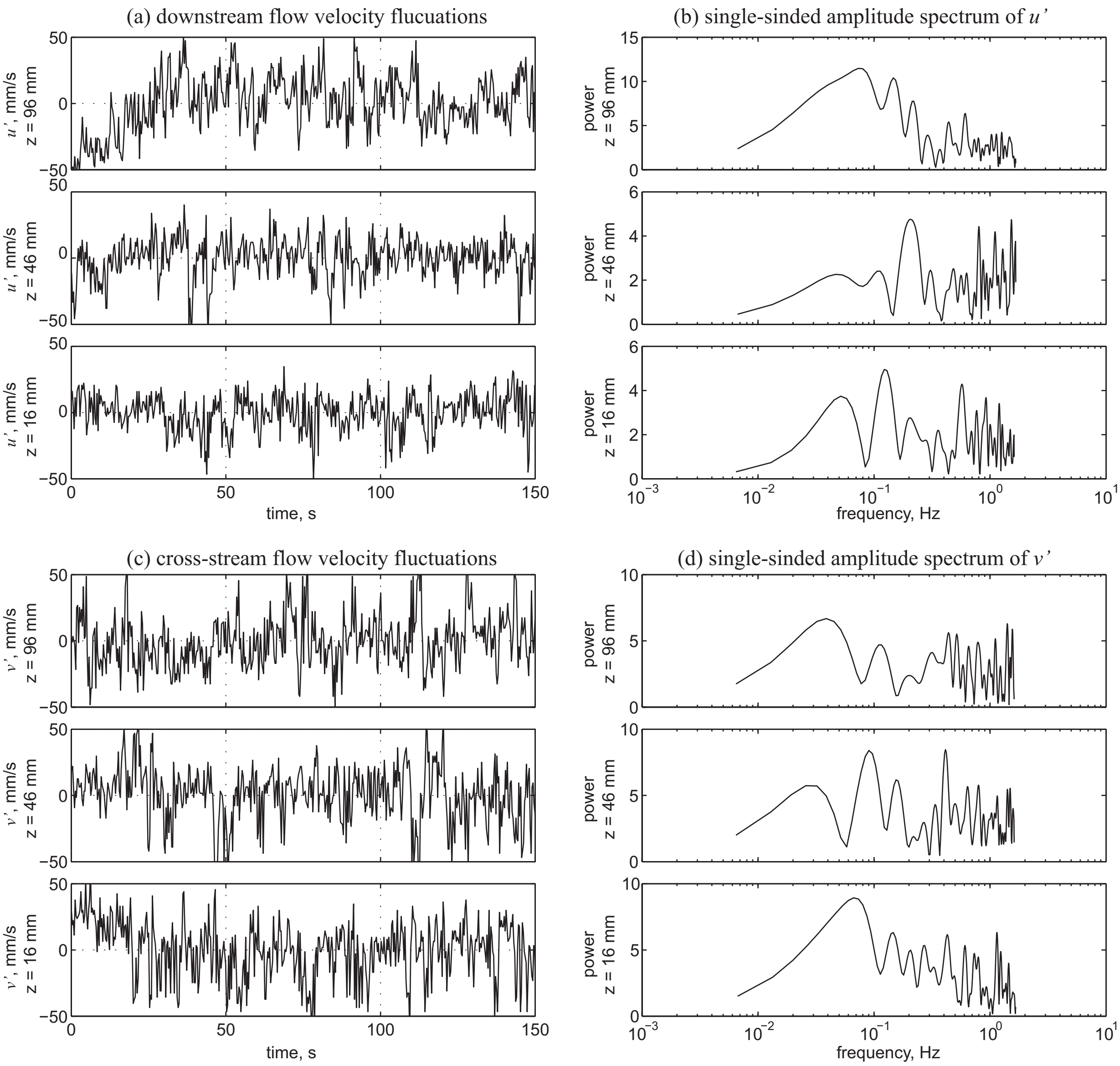

Figure 4. Primary, u', and secondary, v', flow velocity fluctuations (a) and (c) from run V, centred on the midline line of the channel apex and derived from a 5-bin (6 mm) average to reduce instrumental noise in the upper (z = 96 mm), central (z = 46 mm) and lower (z = 16 mm) regions of the flow. Associated single-sided FFT of primary and secondary flow velocity fluctuations signals, respectively (b) and (d), showing the slow and fast scales of turbulent fluctuations observed. The three vertical UDVP locations are denoted by black tick marks in Figure 3.

It is important to note, that this low frequency forcing is not an artefact of the flow input, controlled by an inverter-driven centrifugal pump with fixed discharge. Moreover, the low frequency forcing is unlikely to be attributable to turbulent eddies at the largest vertical scale of the flow. Here turbulent eddy timescales, determined by the ratio of flow depth to downstream flow velocity (Pope, 2000), are

~2 Hz. The long-timescale variations, an order of magnitude larger (<0.2 Hz), drive change in the primary (downstream) flow and thus result in transitions between different secondary flow cell configurations. The different secondary flow cell configurations are recorded in the instantaneous cross-channel measurements of secondary flow, see Figures 5-6 and in the online supplementary material a real-time animation of secondary flow covering 150 s of experimental runs I-IX.

Observed cross-channel patterns captured in the instantaneous measurements of secondary flow are summarised in Figures 5a-i, as a function of basal slope, and Figures 6a-i, as a function of bed roughness. Also plotted is the temporal evolution of the secondary flow field at three different depths, see Figures 5j-l and 6j-l. As in Figure 3 the inner-bank orientated secondary flow was observed to be more predominant with increasing basal slope (Figure 5), or bed roughness (Figure 6). However, in all runs experiments were observed to transition between vertically stacked rotating flow cells with river-normal (towards the inner bank) (see, e.g., Figures 5d and 6g) and river reversed (towards the outer bank) near bed flow behaviour (see, e.g., Figure 5a and 6e). Single stack rotating flow cells were observed, but only with near-bed flow orientated towards the outer-bank. Interestingly the derived streamlines (based on Equation 7) further suggest that instantaneous secondary flow was at times composed of horizontal arrays of multiple rotating cells (see, e.g., Figures 5h and 6f). Steady horizontal arrays of rotating cells are commonly found in open channel flows (e.g., McLelland et al., 1999; Albayrak and Lemmin, 2011). However, although the discharge input is held constant in these density driven flows, the positioning and number of these cells vary temporally and thus are not observed when considering a time averaged description of the flow, Figure 3. The importance of the transition in the arrangement and rotation of secondary flow cells is highlighted in Figures 5j-l and 6j-l. Here it is seen that the magnitude, and orientation, of the near-bed flow velocity naturally vary with the same low frequency period recorded in the down- and cross-stream flow velocity fluctuations, Figure 4.

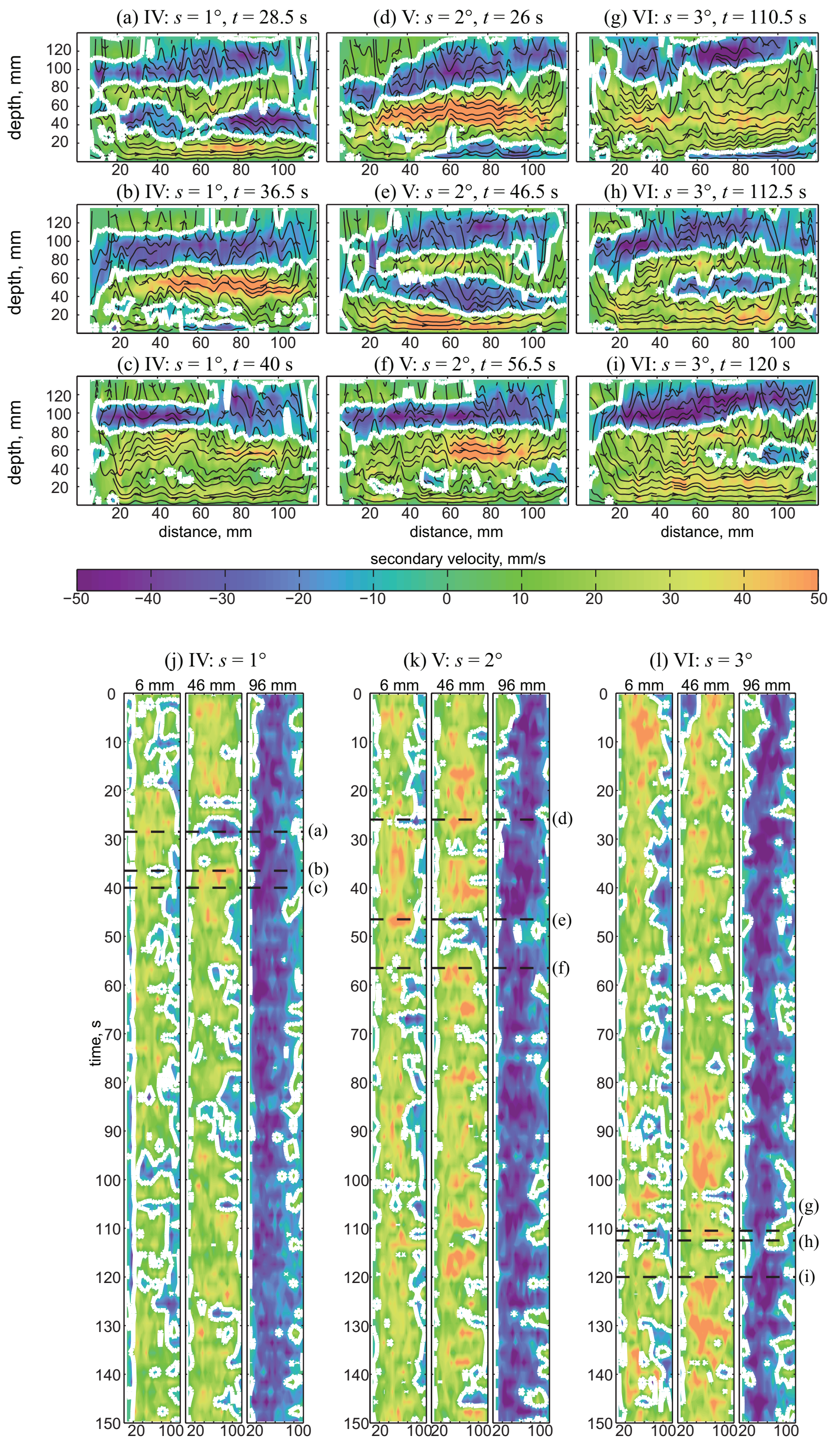

Figure 5. Instantaneous time-slices (a)-(i) and cross channel spatial-slices, (j)-(l) taken at 6, 46 and 96 mm above the bed respectively, of the secondary flow velocity field. Time and spatial slices contrast slopes of 1, 2 and 3 degrees (Runs IV, V and VI respectively where bed particle size d=0.37mm). Flow directed from inner (left) to outer (right) bank is positive. Black lines denote flow streamlines, Equation (7), whilst solid white lines denote contours of zero velocity. Black dashed lines on (j)-(l) denote temporal locations of subplots (a)-(i).

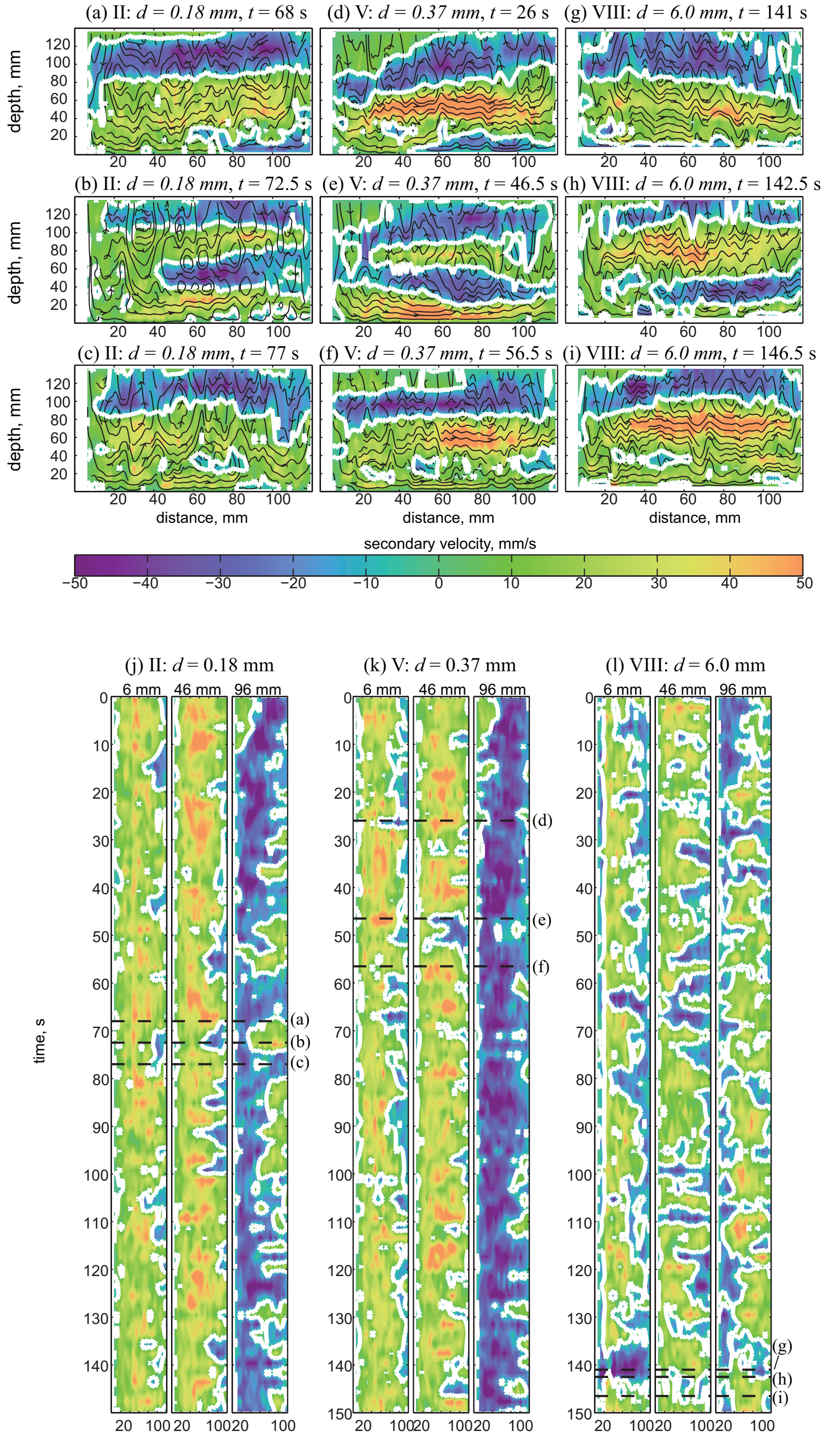

Figure 6. Instantaneous time-slices (a)-(i) and cross channel spatial-slices, (j)-(l) taken at 6, 46 and 96 mm above the bed respectively, of the secondary flow velocity field. Time and spatial slices contrast bed roughness, where bed particle size d = 0.19, 0.37 and 6 mm (Runs II, V and VIII respectively on slope s=2 degrees). Flow directed from inner (left) to outer (right) bank is positive. Black lines denote flow streamlines (Equation 7) whilst solid white lines denote contours of zero velocity. Note the blanking distance at the base of experiment VIII caused by the 6 mm glass sphere bed-roughness elements. Black dashed lines on (j)-(l) denote temporal locations of subplots (a)-(i).

4 Discussion

4.1 Correlation of net secondary flux and near bed secondary flow velocity.

Based on the conservation of momentum in vertically stratified density driven flows, previous research has shown that near bed radial velocity, in steady flow conditions, is proportional to the net radial fluid flux, as a consequence of conservation of fluid mass, see Figure 1 and Dorrell et al. (2013). From the experimental data presented herein we directly investigate the relationship between the time average near bed flow velocity and radial flux, Figure 7. It is found that at 10% flow height there is a strong positive correlation between near-bed radial dimensionless flow velocity and radial fluid flux (see Equation 1), with a correlation coefficient, r^2, of ~0.7 (Figure 7b). The positive correlation shows that with increasing flux the outer-bank orientated radial flow velocity increases, as predicted by Dorrell et al., (2013). However, at 1% flow height, Figure 7a, the positive correlation predicted by Dorrell et al., (2013) between radial flux and near-bed radial flow velocity, while still present is much weaker, and the correlation coefficient, r^2, drops to ~0.3. This decrease in correlation between the near-bed flow velocity and the net radial fluid flux may be explained by the observed instability of the flow. The observed secondary flow switches from single-cell near bed river-reversed to stacked-cell river-normal flow, e.g. helical couplets (see Figures 5-6, and supplementary online animation). This suggests that the flow is close to, but above, the upper transition curve in Figure 1, but that flow perturbations are sufficiently large to decrease the radial fluid and suspended material fluxes below the curve. The inference from the experiments is thus that, even under nominally steady flow conditions, the configuration of the secondary flow structure of density driven flow in sinuous channels may be unstable. The stability of the flow will depend on the magnitude of the perturbations made by the low-frequency forcings in river-normal to river-reversed phase-space, Figure 1. If the flow is close to a river-reversed to river-normal transitional point, small perturbations will have a large effect on secondary flow structure and thus turbulent mixing.

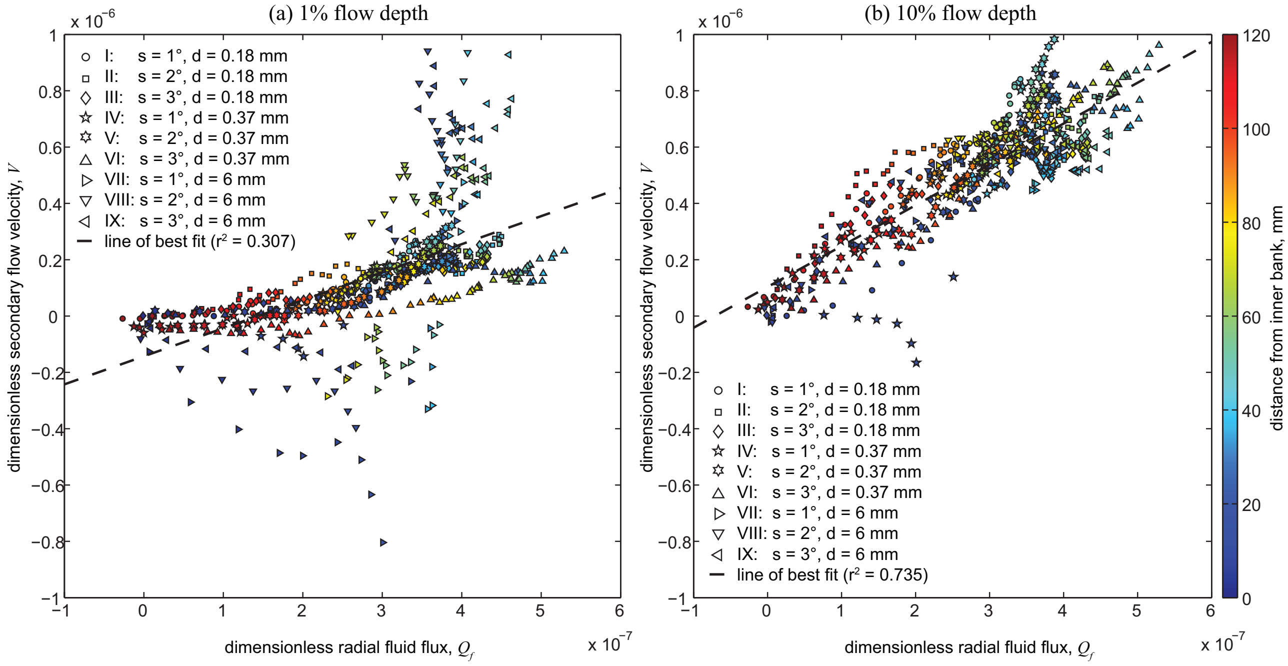

Figure 7. Dimensionless near-bed secondary flow velocity, V, at (a) 1% and (b) 10% of flow depth above the bed roughness elements, as derived from interpolated UDVP data, plotted as a function of dimensionless radial fluid flux Q_f (Equation 1).

From Figure 7 it is also noted that the magnitude of the, positive, radial flux (and thus near bed radial velocity) decreases as a distance from the inner bank. This is an expected result as flow near the inner bank is free to move towards the outer-bank, whilst flow near the outer-bank is limited by the fully constraining sidewalls used in these experiments. In contrast to the experiments, for flows only partially confined by a channel, there may be significant overspill and thus net radial transport may be significant across the entire channel. However, even in confined channels there is significant flow towards the outer-bank at the bend apex, meaning that superelevation is still increasing towards a maximum past the bend apex. Post maximum superelevation radial fluxes must be reversed as the flow-ambient fluid interface reverts to its normal position, and in partially confining channels overspill is switched off. Therefore, regardless of channel type, the location of the superelevation maximum is critical to understanding change in net radial flux around the bend, e.g. from inner bank to outer or vice-versa, and thus the behaviour of the near-bed radial flow velocity. It therefore dictates the reaches of the bend where sediment is transported towards the outer- and inner-bank respectively and its average post apex location may explain why point bars are formed further along bends in seafloor channels than in comparable fluvial systems (Peakall et al., 2007; Amos et al., 2010; Darby and Peakall, 2012; Peakall and Sumner, 2015). Moreover, temporal variations in the position of the superelevation maximum are directly linked to temporal variations of the radial velocity profile at the bend apex. For example, if the position of the superelevation maximum moves downstream away from the bend apex, radial flux, and thus the propensity for outer bank orientated secondary flow, is likely to increase. In contrast, upstream movement of the superelevation maximum will lead to a reduction in outer bank orientated secondary flow.

4.2 Implications of unstable secondary flow for mixing in sinuous channels

A key implication of the observed instability of secondary flow cells for sinuous seafloor channels is enhanced turbulent energy production and, turbulent flow induced, vertical sediment mixing. This may be deduced from the long-timescale variations in primary and secondary flow velocity shown in Figure 4. It is noted that, because the flow transitions between different secondary flow cell arrangements, periodical variations in the cross-stream flow velocity fluctuations are not in phase. That is to say negative fluctuations lower in the flow may correspond to positive fluctuations higher up in the flow or vice-versa. A consequence of variation of cross-stream flow circulation is variation of the vertical position of the flow velocity maximum, Figure 8a. The cross-channel location of the flow velocity maximum is also likely to vary as a function of time, but is not recorded herein. The vertical location of the flow velocity maximum at the centreline of the channel at the bend apex is forced at the same frequency to the long-term fluctuations in primary and secondary flow, Figure 8b.

Production of turbulent kinetic energy, and thus mixing through turbulent fluid motion, is modelled by turbulent shear stresses, where shear may be assumed proportional to the velocity gradient (Pope, 2000). In steady flows this may lead to a reduction of turbulence and turbulent mixing and diffusion (i.e. the slow diffusion zone) at the velocity maximum. However, although the experimental flows generated here have a steady state input the flows themselves have inherent temporal variations. These fluctuations mean that, whilst at an instance in time the velocity gradient is zero at the local velocity maximum, the velocity gradient at the average velocity maximum is not zero, Figure 8c.

Unsurprisingly the driving frequencies of variation in velocity gradient at the flow velocity maximum are similar to the driving frequencies of primary and secondary flow fluctuation, Figures 4 and 8d.

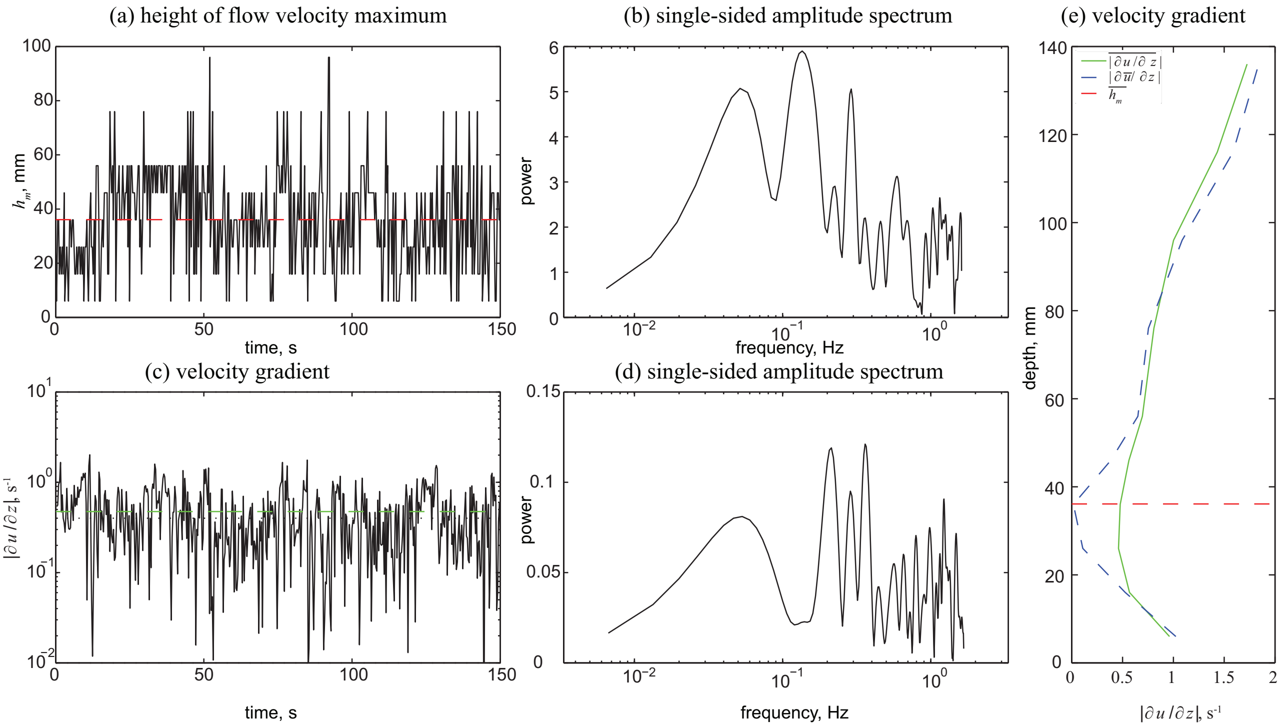

Figure 8. Temporal variations, from experimental run V, of: the height of the velocity maximum, h_m (a); and the absolute velocity gradient estimated, $|\partial u/\partial z|$, at $z = h_m$ (c). (b) and (d) respectively plot the single-sided amplitude spectrum of the fluctuations of $h_m - \overline{h_m}$ and $|\partial u/\partial z| - \overline{|\partial u/\partial z|}$. (e) absolute values of the average velocity gradient, $\overline{|\partial u/\partial z|}$ (green solid curve), compared to the gradient of the average velocity, $\partial \bar{u}/\partial z$ blue dashed curve), as a function of flow depth. In (a) and (e) the average depth of the flow velocity maximum is denoted by a red dashed curve.

A direct consequence of this is that, near the flow velocity maximum, the gradient of the average flow velocity is not equal to the average flow velocity gradient. That is to say that unstable secondary flow cells drive long-timescale variation in the zone of low shear and low turbulent mixing near the flow velocity maximum, diffusing its effects over a wide central region of the flow, see Figure 8e and Keevil et al. (2006). Furthermore, timescales over which sediment in suspension responds to changes in flow conditions are large, scaling with flow depth over settling velocity (Dorrell and Hogg, 2011). Thus, sediment response timescales may be much greater than hydrodynamic timescales associated with unstable secondary flow. Therefore, enhanced mixing by unstable secondary flow will reduce stratification, and thus help to maintain sediment transport capacity of density driven flows (Dorrell et al., 2014). In particular, the implication is that this new mixing mechanism will work alongside those previously identified — stable secondary circulation (Keevil et al., 2006), run-up and superelevation at bends (Straub et al., 2011), and internal hydraulic jumps (Dorrell et al., 2016) — to reduce the vertical variation in sediment concentration and enhance run-out distances.

4.3 A new interpretation of secondary flow dynamics in submarine channels.

Assuming the processes observed in the experiments reported herein are transferable to real oceanic density driven flows, it is proposed that the secondary component of density driven flow in sinuous seafloor channels varies dynamically. The dynamic variation in secondary flow structure is observed to occur at time-scales larger than natural, flow-depth scale, turbulent eddies. It is therefore proposed that the orientation of secondary flow cells within sinuous channel systems can be unstable.

A key question is what mechanism controls flow instability, and thus the perturbations between secondary flow cell states, observed within the experiments? One possible mechanism is that, as turbulent flow is drawn around the meander apex, large-scale coherent vortices are shed (Uijttewaal, 2014) from horizontal recirculation zones, as observed in open-channel flow (Hickin, 1978; Ferguson et al., 2003). This vortex shedding naturally results in perturbations to the mean flow travelling around the meander bend. Moreover in the case of density currents, because of the low-density differences between the ambient fluid and flow, small perturbations may have relatively large impact on flow dynamics; see Figure 1 and Dorrell et al. (2013). Furthermore, separation zones are more likely in submarine channels than in rivers as a result of the prevalence of river-reversed secondary circulation that keeps flows outwardly directed for longer around the bend (Peakall and Sumner, 2015). Such separation zones have been widely recognised in submarine channel experiments and simulations (Straub et al., 2008, 2011; Ezz et al., 2013; Janocko et al., 2013; Basani et al., 2014).

The vortex shedding frequency, f, of flow past an obstacle may be estimated

(8) $$f \approx 0.10\frac{U}{r},$$

where r is the radius of the flow obstacle and U the characteristic flow velocity past it (Bearman, 1969). Taking r as the inner radius of the channel (r=0.1 m, Figure 2) and considering experiment V, where the time and maximum flow velocity ~0.1 m/s at ~46 mm above the bed (Figure 3), the predicted vortex shedding frequency is f~0.1 Hz. This is in quantitative agreement to the observed low frequency in; the downstream and cross-stream velocity fluctuations (Figure 4); variation in the height of the velocity maximum (Figure 8); and turbulence production through shear (Figure 8). Scaling this to real-world channels and flows, where channel bend radii are ~0.5-15 km and flow velocities are ~1-10 m/s (Pirmez and Imran, 2003; Peakall and Sumner, 2015), the shedding frequency is ~8-2500 minutes.

4.4 Implications for sediment transport and submarine channel evolution

A key implication of the observed fluctuations in the structure of secondary flow cells is that the reversals in basal flow direction lead to a net reduction in cross-stream sediment transport at a given point around the bend. Furthermore the analysis of these reversals in terms of the vortex shedding frequency, f, suggests that they will become more frequent in tighter bends; i.e. f increases as r decreases, see Equation (8). Thus, vortex shedding is expected to progressively increase as bend amplitude increases from an initially approximately straight planform (e.g., see Peakall et al., 2000a, b). In this case, net cross-stream sediment transport will systematically reduce as bends grow, in turn suggesting that this may lead to a reduction in the rate of bend growth. This change in bend growth rate agrees with observations from submarine channel-levee systems where bend growth progressively decreases as a function of aggradation (Peakall et al., 2000a, b; Jobe et al., 2016).

Eventually submarine channels reach a point where there is a near cessation of planform movement (termed ossification) and are dominated by vertical aggradation (Peakall et al., 2000a; Wynn et al., 2007; Jobe et al., 2016). This contrasts with river channels that, although showing a rapid decrease in outer bend erosion rates as bend curvature tightens through outer bank flow separation (Blanckaert, 2011; Blanckaert et al., 2013) and increased flow resistance (Hickin and Nanson, 1975), do not reach a point where bend migration ceases (Hickin and Nanson, 1975 and 1984). Peakall et al., (2000a) first postulated that additional processes in submarine channels, or variations in these processes, may reinforce this fluvial-type stability criterion for bend stability, leading to the cessation of planform movement. Here we suggest that the observation herein that net sediment transport at a given point on a bend decreases with increasing bend curvature due to periodic changes in the structure of secondary flows, may provide the additional forcing for channel bends to reach stability. Peakall et al., (2000a, p.446) earlier raised this possibility: "if the intensity or frequency of flow-cell reversal is linked to the curvature of the meander bend, there may be a negative feedback mechanism that serves to stabilize meanders".

A number of other mechanisms have however been postulated for the near cessation of planform movement in submarine channels, including: i) clay hysteresis where the shear stress required to erode the clay is much higher than that to deposit, ii) climate-induced flow size reduction, iii) changes in flow type, and, iv) a balance between equilibrium flows depositing at the inner bank and disequilibrium flows depositing at the outer bank (Peakall et al., 2000a, Wynn et al., 2007; Kane et al., 2008; Nakajima et al., 2009; Amos et al., 2010). Jobe et al., (2016) identify that this reduction in bend growth is common to submarine channels irrespective of tectonic setting or other allogenic drivers, and thus suggest that the key control(s) is autogenic. This suggests that earlier hypotheses that planform cessation is related to climate induced flow size reduction, or to changes in flow type, are untenable. Similarly, variations in flow volume and thus equilibrium flows may be less important in sinuous submarine channels since the channels act to regulate the size of flows that traverse them through channel overspill at bends (Straub et al., 2008; Amos et al., 2010). Clay hysteresis will occur in a variety of systems such as rivers, tidal channels, and submarine channels, albeit that submarine channels and their associated levees can be an order of magnitude larger than in rivers (Konsoer et al., 2013) thus potentially strengthening the effect. Given the aforementioned analysis, the evidence presented here for changes in secondary flow cells and their influence on net sediment transport, as a function of bend curvature, appears the most plausible mechanism, in combination with the known increase in resistance to flow as bends tighten, for the observed stabilisation of submarine channel planforms.

An additional implication of the present work is that if the shedding frequency is low, and the net bed aggradation rate is high, then it may be possible for submarine channel bend deposits to preserve both inner bank and outer bank directed sedimentary structures (in and around the bend apex position), reflecting periodic changes between river-normal and river-reversed secondary flows. Significant variability in palaeocurrent directions, with inward and outward directed examples, has been recorded in submarine channel point bar deposits (Pyles et al., 2012).

5 Conclusions

Previous research, based on the analysis of individual time-slice or temporally averaged flow data, has lead to a model of stable secondary flow cells in submarine channel flows with continuous steady input. However, here novel experimental observations and analysis are presented that show that the velocity fields of these pseudo-steady density currents in sinuous channels can be temporally unstable. This flow instability is manifested as long-time scale variation in both primary (downstream) and secondary (cross-stream) flow fields measured at the apex of a channel bend. Further, it is demonstrated that these instabilities can enhance cross-channel flow and vertical mixing, and thus mitigate the previously proposed effects of the slow diffusion zone in inhibiting mixing past the velocity maximum in density driven flows. It is postulated that the temporal instability of such flows is driven by vortex shedding, in a similar manner as observed in turbulent flows past an obstacle. The importance of flow instability is highlighted by the flow switching between different secondary flow states, alternating between single secondary cells with outer bank directed basal flow and twin-stacked cells with either inner or outer bank directed basal flow. The proposed mechanism suggests that flow instability driven alternation of near bed secondary flow direction leads to a progressive reduction of net cross-channel bedload transport as a function of tightening bend curvature during bend growth. Ultimately we postulate that this may cause termination of net cross-channel bedload transport and therefore explain the eventual stabilisation of sinuous channels in subaqueous settings.

Acknowledgements

This research was supported by award NE/F020120/1 from the Natural Environmental Research

Council (NERC). We also thank NERC for supporting the Sorby Environmental Fluid Dynamics Laboratory at the University of Leeds where the experiments were undertaken. We thank an anonymous reviewer and Editor James Plater for their constructive reviews.

References

Abad, J.D., Sequeiros, O.E., Spinewine, B., Pirmez, C., Garcia, M.H., Parker, G., 2011. Secondary current of saline underflow in a highly meandering channel: experiments and theory. Journal of Sedimentary Research 81, 787-813.

Albayrak, I., Lemmin, U., 2011. Secondary currents and corresponding surface velocity patterns in a turbulent open-channel flow over a rough bed. Journal of Hydraulic Engineering 137, 1318-1334.

Amos, K.J., Peakall, J., Bradbury, P.W., Roberts, M., Keevil, G., Gupta, S., 2010. The influence of bend amplitude and planform morphology on flow and sedimentation in submarine channels. Marine and Petroleum Geology 27, 1431–1447. http://dx.doi.org/10.1016/j.marpetgeo.2010.05.004

Baines, P.G., 1998. Topographic Effects in Stratified Flows. Cambridge University Press, Cambridge, UK.

Basani, R., Janocko, M.J., Cartigny, M.J.B., Hansen, E.W.M., Eggenhuisen, J.T., 2014. MassFlow-3D™ as a simulation tool for turbidity currents: some preliminary results. In: Martinius, A.W., Ravnås, R., Howell, J.A., Steel, R.J., Wonham, J.P. (Eds.), From Depositional Systems to Sedimentary Successions on the Norwegian Continental Margin. International Association of Sedimentologists Special Publication 46, pp. 587–608.

Bearman, P.W., 1969. On vortex shedding from a circular cylinder in the critical Reynolds number regime. Journal of Fluid Mechanics 37, 577-585.

Best, J.L., Kirkbride, A.D., Peakall, J., 2001. Mean flow and turbulence structure of sediment-laden gravity currents: New insights using Ultrasonic Doppler Velocity Profiling. In: McCaffrey, W.D., Kneller, B.C., Peakall, J., (Eds.), Particulate Gravity Currents. International Association of Sedimentologists Special Publication 31, pp. 157-172.

Blanckaert, K., 2011. Hydrodynamic processes in sharply-curved river bends and their morphological implications. Journal of Geophysical Research – Earth Surface 116, F01003.

Blanckaert, K., Kleinhans, M.G., McLelland, S.J., Uijttewaal, W.S.J., Murphy, B.J., van de Kruijs, A., Parsons, D.R., Chen, Q., 2013. Flow separation at the inner (convex) and outer (concave) banks of constant-width and widening open-channel bends. Earth Surface Processes and Landforms, 38, 696-716.

Buckee, C., Kneller, B., Peakall, J., 2001. Turbulence structure in steady, solute-driven gravity currents. In: McCaffrey, W.D., Kneller, B.C., Peakall, J., (Eds.), Particulate Gravity Currents. International Association of Sedimentologists Special Publication 31, pp. 173-187.

Corney, R.K., Peakall, J., Parsons, D.R., Elliott, L., Amos, K.J., Best, J.L., Keevil, G.M., Ingham, D.B., 2006. The orientation of helical flow in curved channels. Sedimentology 53(2), 249-257.

Corney, R.K., Peakall, J., Parsons, D.R., Elliott, L., Best, J.L., Thomas, R.E., Keevil, G.M, Amos, K.J., 2008. Reply to discussion of Imran et al. on "The orientation of helical flow in curved channels" by Corney et al., Sedimentology, 53, 249–257. Sedimentology 55, 241-247.

Cossu, R., Wells, M.G., 2010. Coriolis forces influence the secondary circulation of gravity currents flowing in large-scale sinuous submarine channel systems. Geophysical Research Letters 37, L17603.

Cossu, R., Wells, M.G., 2013. The evolution of submarine channels under the influence of Coriolis forces; experimental observations of flow structures. Terra Nova 25, 67–71. http://dx.doi.org/10.1111/ter.12006.

Cossu, R., Wells, M.G., Peakall, J., 2015. Latitudinal variations in submarine channel sedimentation patterns: the role of Coriolis forces. Journal of the Geological Society 172, 161-174.

Covault, J.A., 2011. Submarine fans and canyon-channel systems: a review of processes, products, and models. Nature Education. Knowledge 3, 4.

Darby, S.E., Peakall, J., 2012. Modelling the equilibrium bed topography of submarine meanders that exhibit reversed secondary flows. Geomorphology 163–164, 99–109. http://dx.doi.org/10.1016/j.geomorph.2011.04.050.

Dorrell, R.M., Hogg, A.J., 2011. Length and time scales of response of sediment suspensions to changing flow conditions. Journal of Hydraulic Engineering 138, 430-439.

Dorrell, R.M., Darby, S.E., Peakall, J., Sumner, E.J., Parsons, D.R., Wynn, R.B., 2013. Superelevation and overspill control secondary flow dynamics in submarine channels. Journal of Geophysical Research: Oceans 118, 3895-3915.

Dorrell, R.M., Darby, S.E., Peakall, J., Sumner, E.J., Parsons, D.R., Wynn, R.B., 2014. The critical role of stratification in submarine channels: Implications for channelization and long runout of flows. Journal of Geophysical Research: Oceans 119, 2620-2641.

Dorrell, R.M., Burns, A.D., McCaffrey, W.D., 2015. The inherent instability of leveed seafloor channels. Geophysical Research Letters 42, 4023-4031.

Dorrell, R.M., Peakall, J., Sumner, E.J., Parsons, D.R., Darby, S.E., Wynn, R.B., Özsoy, E., Tezcan, D., 2016. Flow dynamics and mixing processes in hydraulic jump arrays: Implications for channel-lobe transition zones. Marine Geology 381, 181-193.

Ezz, H., Imran, J., 2014. Curvature-induced secondary flow in submarine channels. Environmental Fluid Mechanics 14, 343-370.

Ezz, H., Cantelli, A., Imran, J., 2013. Experimental modeling of depositional turbidity currents in a sinuous submarine channel. Sedimentary Geology, 290, 175–187.

Ferguson, R.I., Parsons, D.R., Lane, S.N., Hardy, R.J., 2003. Flow in meander bends with recirculation at the inner bank. Water Resources Research 39, 1322-1333, doi:10.1029/2003WR001965.

Fukushima, Y., Parker, G., Pantin, H.M., 1985. Prediction of ignitive turbidity currents in Scripps Submarine Canyon. Marine Geology 67, 55-81.

Garcia, M., Parker, G., 1993. Experiments on the entrainment of sediment into suspension by a dense bottom current. Journal of Geophysical Research: Oceans 98, 4793-4807.

Greenhill, R.K., Sellin, R.H.J., 1993. Development of a simple method to predict discharges in compound meandering channels. Proceedings of the Institute of Civil Engineers, Water Maritime Energy 101, 37–44.

Hickin, E.J., 1978. Mean flow structure in meanders of the Squamish River, British Columbia. Canadian Journal of Earth Sciences 15, 1833-1849.

Hickin, E.J., Nanson, G.C., 1975. The character of channel migration on the Beatton River, Northeast British Columbia, Canada. Geological Society of America Bulletin 86, 487–494.

Hickin, E.J., Nanson, G.C., 1984. Lateral migration rates of river bends. Journal of Hydraulic Engineering 110, 1557–1567.

Imran, J., Parker, G., Pirmez, C. 1999. A nonlinear model of flow in meandering submarine and subaerial channels. Journal of Fluid Mechanics 400, 295-331.

Janocko, M., Cartigny, M.B.J., Nemec, W., Hansen, E.W.M., 2013. Turbidity current hydraulics and sediment deposition in erodible sinuous channels: laboratory experiments and numerical simulations. Marine and Petroleum Geology 41, 222–249.

Jobe, Z.R., Howes, N.C., Auchter, N.C., 2016. Comparing submarine and fluvial channel kinematics: Implications for stratigraphic architecture. Geology 44, 931-934.

Kane, I.A., McCaffrey, W.D., Peakall, J., 2008. Controls on sinuosity evolution within submarine channels. Geology 36, 287–290.

Kassem, A., Imran, J., 2004. Three-dimensional modeling of density current, II. Flow in sinuous confined and unconfined channels. Journal of Hydraulic Research 42, 591–602.

Keevil, G.M., Peakall, J., Best, J.L., Amos, K.J., 2006. Flow structure in sinuous submarine channels: velocity and turbulence structure of an experimental submarine channel. Marine Geology 229, 241-257.

Keevil, G.M., Peakall, J., Best, J.L., 2007. The influence of scale, slope and channel geometry on the flow dynamics of submarine channels. Marine and Petroleum Geology 24, 487-503.

Kneller, B., Buckee, C., 2000. The structure and fluid mechanics of turbidity currents: a review of some recent studies and their geological implications. Sedimentology 47, 62-94.

Kneller, B.C., Bennett, S.J., McCaffrey, W.D., 1999. Velocity structure, turbulence and fluid stresses in experimental gravity currents. Journal of Geophysical Research 104, 5381-5391.

Konsoer, K., Zinger, J., Parker, G., 2013. Bankfull hydraulic geometry of submarine channels created by turbidity currents: relations between bankfull channel characteristics and formative flow discharge. Journal of Geophysical Research: Earth Surface 118, 216–228.

Menard, H.W., Ludwick, J.C., 1951. Applications of hydraulics to the study of marine turbidity currents. In: Hough, J.L., (Ed.) Turbidity Currents and the Transportation of Coarse Sediments to Deep Water. Society of Economic Paleontologists and Mineralogists Special Publication 2, pp. 2–13.

McLelland, S.J., Ashworth, P.J., Best, J.L., Livesey, J.R., 1999. Turbulence and secondary flow over sediment stripes in weakly bimodal bed material. Journal of Hydraulic Engineering 125, 463-473.

Nakajima, T., Peakall, J., McCaffrey, W.D., Paton, D.A., Thompson, P.J.P., 2009. Outer-bank bars: a new intra-channel architectural element within sinuous submarine slope channels. Journal of Sedimentary Research 79, 872–886.

Nezu, I., Nakagawa, H., 1993. Turbulence in Open Channel Flows. Balkema, Rotterdam, The Netherlands (279 pp.).

Parker, G., Garcia, M.H., Fukushima, Y., Yu, W., 1987. Experiments on turbidity currents over an erodible bed. Journal of Hydraulic Research 25, 123–147.

Peakall, J., Sumner, E.J., 2015. Submarine channel flow processes and deposits: A process-product perspective. Geomorphology 244, 95-120.

Peakall, J., McCaffrey, W.D., Kneller, B.C., 2000a. A process model for the evolution, morphology, and architecture of sinuous submarine channels. Journal of Sedimentary Research 70, 434–448.

Peakall, J., McCaffrey, W.D., Kneller, B.C., Stelting, C.E., McHargue, T.R., Schweller, W.J., 2000b. A process model for the evolution of submarine fan channels: implications for sedimentary architecture. In: Bouma, A.H., Stone, C.G. (Eds.), *Fine-grained Turbidite Systems.* American Association of Petroleum Geology Memoir 72/Society for Sedimentary Geology Special Publication 68, pp. 73–88.

Peakall, J., Amos, K.J., Keevil, G.M., Bradbury, P.W., Gupta, S., 2007. Flow processes and sedimentation in submarine channel bends. Marine and Petroleum Geology 24(6), 470-486.

Pirmez, C., Imran, J., 2003. Reconstruction of turbidity currents in Amazon Channel. Marine and Petroleum Geology 20, 823–849.

Pope, S.B., 2000. Turbulent flows, Cambridge University Press, Cambridge, UK.

Pyles, D.R., Tomasso, M., Jennette, D.C., 2012. Flow processes and sedimentation associated with erosion and filling of sinuous submarine channels. Geology 40, 143–146. http://dx.doi.org/10.1130/G32740.32741.

Rozovskii, I., 1957. Flow of Water in Bends in Open Channels, Academy of Science of the Ukrainian SSR, Israel Program Scientific Translations, Jerusalem.

Sarkar, S., Scotti, A., 2017. From topographic internal gravity waves to turbulence. Annual Review of Fluid Mechanics, 49, 195-220.

Sellin, R.H.J., Ervine, D.A., Willetts, B.B., 1993. Behaviour of meandering two-stage channels. Proceedings of the Institute of Civil Engineers, Water Maritime Energy 101, 99–111.

Straub, K.M., Mohrig, D., McElroy, B., Buttles, J., Pirmez, C., 2008. Interactions between turbidity currents and topography in aggrading sinuous submarine channels: A laboratory study. Geological Society of America Bulletin 120, 368-385.

Straub, K.M., Mohrig, D., Buttles, J., McElroy, B., Pirmez, C., 2011. Quantifying the influence of channel sinuosity on the depositional mechanics of channelized turbidity currents: A laboratory study. Marine and Petroleum Geology 28, 744-760.

Thorne, C.R., Zevenbergen, L.W., Pitlick, J.C., Rais, S., Bradley, J.B., Julian, P.Y., 1985. Direct measurement of secondary currents in a meandering sand-bed river. Nature 316, 746–747.

Uijttewaal, W.S.J.., 2014. Hydrodynamics of shallow flows: application to rivers. Journal of Hydraulic Research 52, 157-172.

Wynn, R.B., Cronin, B.T., Peakall, J., 2007. Sinuous deep-water channels: genesis, geometry and architecture. Marine and Petroleum Geology 24, 341–387.